

A statistical state dynamics based theory for the formation and equilibration of Saturn's North Polar Jet

Brian F. Farrell

School of Engineering and Applied Science, Harvard University

Petros J. Ioannou*

Department of Physics, National and Kapodistrian University of Athens

(Dated: May 18, 2022)

Coherent jets containing most of the kinetic energy of the flow are a common feature in observations of atmospheric turbulence at planetary scale. In the gaseous planets these jets are maintained by incoherent turbulence excited by convection on scales small relative to the jet scale. Large scale coherent waves are sometimes observed to coexist with the coherent jets and a prominent example of this phenomenon is the distortion of Saturn's North Polar Jet (NPJ) into a distinct hexagonal form. Observations of the large scale jet/wave coexistence regime raises the question of identifying the mechanism responsible for forming and maintaining this turbulent state. The coherent planetary scale component of the turbulence arises and is maintained by interaction with the incoherent small-scale turbulence component. It follows that theoretical understanding of the dynamics of the jet/wave /turbulence coexistence regime is facilitated by employing a statistical state dynamics (SSD) model in which the interaction between coherent and incoherent components is explicitly represented. In this work a second order closure implementation of a two-layer beta-plane SSD is used to develop a theory that accounts for the structure and dynamics of the NPJ. Analysis with this model of the jet/wave/turbulence regime dynamics reveals that jet formation is controlled by the effective value of β and the required value of this parameter for correspondence with observation is obtained. As this is a robust prediction it is taken as an indirect observation of a deep poleward sloping stable layer beneath the NPJ. The slope required is obtained from observations of NPJ structure as is the small scale turbulence excitation required to maintain the jet. The observed jet structure is then predicted by the theory as is the wave six disturbance. This wave, which is identified with the least stable mode of the equilibrated jet, is shown to be primarily responsible for equilibrating the jet with the observed structure and amplitude.

INTRODUCTION

Coherent structures emergent from small scale turbulence are often observed in planetary atmospheres with the zonal jets of the gaseous planets being familiar examples [1–3].

While this phenomenon of spontaneous large scale jet organization from small scale turbulence has been extensively investigated in both observational and theoretical studies [4–17] the physical mechanism underlying it remains controversial. The prominence of jets in planetary turbulence is in part due to the jet being a nonlinear stationary solution of the dynamics in the limit of vanishing dissipation and therefore not disrupted by nonlinear advective processes. However, this observation is insufficient by itself to serve as an explanation for the observed jets for three reasons. First, strong jets typically assume a characteristic structure for a given set of system parameters, while any zonally symmetric flow is a fixed point of the inviscid dynamics. Second, nonlinear stationary states lack a mechanism of maintenance against dissipation and so can not explain the fact that the observed jets, which are not maintained by coherent external forcing such as by an imposed pressure gradient, persist much longer than the dissipation time scale. Third, planetary jets commonly appear to be unstable;

for example, the north polar jet (NPJ) of Saturn robustly satisfies Rayleigh's necessary condition for barotropic instability in a dissipationless stationary flow [18, 19], and the barotropic instability of this jet has been verified by eigenanalysis [20].

The aforementioned considerations imply that a comprehensive theory for the existence of large scale jets in the atmospheres of the gaseous planets and in particular Saturn's NPJ must provide a mechanism for the formation and maintenance of the jet from incoherent turbulence, the particular structure assumed by the jet and its stability. In addition to these the case of the NPJ also requires that the theory account for the prominent coherent wave six structure that distorts the jet into a distinct hexagonal form.

The primary mechanism by which jets are maintained in turbulent flow is upgradient perturbation momentum flux resulting from straining of the perturbation field by the mean jet shear which implies a spectrally nonlocal interaction between the small-scale perturbation field and the large-scale jet. This mechanism has been verified in observational studies of both Jovian and Saturnian atmospheres [21–23], as well as in numerical simulations [9, 10] and in laboratory experiments [24]. This upgradient momentum transfer mechanism has been found to maintain mean jets both in barotropic forced dissipative models

[10, 25] and in baroclinic free turbulence models [8, 26]. Excitation of the observed small scale forced turbulence has been traced to convection in the case of both the Jovian and Saturnian jets [3, 27, 28].

In this work Saturn's NPJ is studied using an implementation of statistical state dynamics (SSD), specifically a closure at second order in a cumulant expansion (cf. [29]) referred to as the stochastic structural stability theory (S3T) system [25]. In S3T the nonlinear terms in the perturbation equation are parameterized by a stochastic excitation rather than being explicitly calculated while the nonlinear interaction of the perturbations with the mean jet are fully retained. For this reason the S3T system may be described as a quasi-linear (QL) model. S3T has been applied previously to the problem of jet formation in barotropic turbulence [30–34] and to jet dynamics in baroclinic turbulence [26, 35]. The S3T system employs an equivalently infinite ensemble in the dynamical equation for the second cumulant and as a result provides an autonomous and fluctuation-free dynamics for the statistical mean turbulent state which greatly facilitates analytic study.

When applying S3T to the study of zonal jets it is appropriate to equate the ensemble mean to the zonal mean by appeal to the ergodic hypothesis. A two-layer model is employed in order to provide the possibility for baroclinic and barotropic dynamics both for the jet itself and for the perturbations that are involved in the equilibration dynamics. One reason this is important is because a barotropic or shallow water model with the observed Rossby radius would not allow the problem freedom to adopt barotropic dynamics. In the event we find that the dynamics is nearly barotropic so that the Rossby radius is not a relevant parameter.

We find that jet formation is tightly controlled by the effective vorticity gradient, β . As this is a robust requirement of the dynamics, the observed jet structure is taken as an indirect observation of this parameter. Saturn's NPJ is similar in structure and amplitude to midlatitude jets on the gaseous planets such as Jupiter's 24° N jet while the planetary value of $\beta_{sat}(74^\circ) = 1.6 \times 10^{-12} \text{ m}^{-1}\text{s}^{-1}$ at the latitude of the NPJ is too weak to stabilize a jet with the observed amplitude, 98.7 m/s which poses an oft remarked dynamical dilemma [18]. Theory and observation can be brought into correspondence by inferring a deep strongly statically stable layer beneath the jet giving rise to the equivalent of a topographic β effect. The β used in the model is then taken to correspond to the contribution to the overall β effect of the planetary and the topographic components of β . With this inferred effective β the observed jet structure accords with the theory.

While the first cumulant provides the structure of the jet, the second determines the planetary scale wave disturbance superposed on the jet. With the inferred value of β and an incoherent turbulence excitation level

consistent with observation this wave is found to have wavenumber six and the amplitude required to produce the observed hexagonal shape of the NPJ. The role of this wave in the dynamics is to equilibrate the jet with the observed velocity structure and amplitude. The nonlinear S3T equilibrium obtained satisfies Rayleigh's necessary condition for instability in both the prograde and retrograde jet and significant interaction between the jet and the incipient instabilities associated with both these vorticity gradient structures is seen. The widely debated enigma of the stability of the NPJ in the face of these strong vorticity gradient sign reversals is resolved by their having been adjusted to (in most cases marginal) stability by the perturbation/mean flow interaction between the first and second cumulants of the S3T dynamics.

APPLYING S3T TO STUDY THE SSD EQUILIBRIA IN A TWO-LAYER MODEL OF SATURN'S ATMOSPHERE

The simplest model that retains the freedom for the dynamics to exploit both baroclinic and barotropic processes is the quasi-geostrophic two-layer model. We choose parameters appropriate for the NPJ of Saturn including planetary vorticity gradient $\beta = df_0/dy$, where f_0 is the planetary vorticity and the derivative is taken at the center of the channel at 74° N. The channel size is L_x in the zonal, x , direction, and L_y in the meridional direction, $y = R\phi$, in which R is the radius of the planet and ϕ is the latitude. The layers are of equal depth, H , with the density of the upper layer, ρ_1 , being less than that of the lower, ρ_2 . Rigid boundaries are imposed at the bottom and the top. The stream function in each layer is denoted ψ_i , with $i = 1$ referring to the top layer and $i = 2$ to the bottom layer. The zonal velocities are $u_i = -\partial_y \psi_i$ and the meridional velocities are $v_i = \partial_x \psi_i$ ($i = 1, 2$). The dynamics is expressed as conservation of potential vorticity, $q_i = \Delta \psi_i + \beta y + (-1)^i \lambda^2 (\psi_1 - \psi_2)$, in which $\lambda^2 = f_0^2/(g'H)$, with $g' = g_{sat}(\rho_2 - \rho_1)/\rho_0$ the reduced gravity associated with the planetary gravitational acceleration g_{sat} and ρ_0 is a characteristic density of the fluid, which is taken here to be $(\rho_1 + \rho_2)/2$ (cf. [36]). The Rossby radius of deformation for baroclinic motions in this two-layer fluid is $L_d = 1/(\sqrt{2}\lambda)$.

The quasi-geostrophic dynamics expressed in terms of the barotropic $\psi = (\psi_1 + \psi_2)/2$ and baroclinic $\theta = (\psi_1 - \psi_2)/2$ streamfunctions is:

$$\partial_t \Delta \psi + J(\psi, \Delta \psi) + J(\theta, \Delta \theta) + \beta \psi_x = -r \Delta \psi + \sqrt{\varepsilon} f_\psi \quad (1a)$$

$$\partial_t \Delta_\lambda \theta + J(\psi, \Delta_\lambda \theta) + J(\theta, \Delta \psi) + \beta \theta_x = -r \Delta_\lambda \theta + \sqrt{\varepsilon} f_\theta, \quad (1b)$$

where $\Delta_\lambda \stackrel{\text{def}}{=} \Delta - 2\lambda^2$. f_ψ and f_θ are random functions with zero mean representing independent vortic-

ity excitations of the fluid by unresolved processes, like convection, with amplitude controlled by ε . The advection of potential vorticity is expressed using the Jacobian $J(f, g) = (\partial_x f)(\partial_y g) - (\partial_y f)(\partial_x g)$. Equations (1) are non-dimensional with length scale $L = 1000$ km and time scale $T = 1$ Earth day implying velocity unit 11.5 ms^{-1} . The coefficient of linear damping is r and this damping may vary with the scale of the motions when appropriate for probing the dynamics controlling jet formation and equilibration. In particular insight can be gained by examining the regime in which the large scale zonal flow is damped at a rate $r_m \ll r_p$ where r_p is the damping rate of the perturbations.

The barotropic and baroclinic streamfunctions are decomposed into a zonal mean (denoted with capitals) and deviations from the zonal mean (referred to as perturbations and denoted with primed small letters):

$$\psi = \Psi + \psi' \quad , \quad \theta = \Theta + \theta' \quad . \quad (2)$$

We denote the barotropic zonal mean flow as $U = -\partial_y \Psi$ and the baroclinic zonal mean flow as $H = -\partial_y \Theta$. Equations for the evolution of the barotropic and baroclinic zonal mean flows are obtained by forming the zonal mean of (1):

$$\partial_t U = \overline{v'q'}_\psi - r_m U \quad (3a)$$

$$\partial_t D_\lambda^2 H = D^2 \overline{v'q'}_\theta - r_m D_\lambda^2 H, \quad (3b)$$

in which the overline denotes zonal averaging, $D^2 \stackrel{\text{def}}{=} \partial_{yy}$ and r_m denotes the linear damping rate of the mean flow. The terms $\overline{v'q'}_\psi \stackrel{\text{def}}{=} \overline{\psi'_x \psi'_{yy} + \theta'_x \theta'_{yy}}$ and $\overline{v'q'}_\theta \stackrel{\text{def}}{=} \overline{\psi'_x D_\lambda^2 \theta' + \theta'_x \psi'_{yy}}$, with $D_\lambda^2 \stackrel{\text{def}}{=} \partial_{yy} - 2\lambda^2$, are respectively the Reynolds stress divergence forcing of the barotropic and baroclinic mean flow or equivalently the barotropic and baroclinic vorticity flux. Vorticity fluxes are referred to as upgradient if they have the tendency to reinforce the mean flow so that e.g. $\int_0^L dy \overline{U v'q'}_\psi > 0$, otherwise they are termed downgradient.

The evolution equations for the perturbations are:

$$\begin{aligned} \partial_t \Delta \psi' + U \partial_x \Delta \psi' + H \partial_x \Delta \theta' + (\beta - D^2 U) \partial_x \psi' - \\ D^2 H \partial_x \theta' = -r_p \Delta \psi' - J(\psi', \Delta \psi')' - J(\theta', \Delta \theta')', \quad (4a) \\ \partial_t \Delta \lambda \theta' + H \partial_x \Delta \psi' + U \partial_x \Delta \lambda \theta' + (\beta - D^2 U) \partial_x \theta' - \\ D_\lambda^2 H \partial_x \psi' = -r_p \Delta \lambda \theta' - J(\psi', \Delta \lambda \theta')' - J(\theta', \Delta \psi')', \quad (4b) \end{aligned}$$

with the prime Jacobians denoting the perturbation-perturbation interactions,

$$J(A, B)' = J(A, B) - \overline{J(A, B)}. \quad (5)$$

Equations (3) and (4) comprise the non-linear system (NL) that governs the two layer baroclinic flow. Dissipa-

tion of the mean at rate r_m and of the perturbations at a lower rate, r_p , in (3) and (4) is consistent with parameterizing diffusion while retaining the simplicity of linear damping. More importantly, it allows us to explore the dynamically interesting regime $r_m = 0$ in which the equilibration of the jet by nonlinear interaction with the perturbations is independent of jet damping.

We impose periodic boundary conditions on Ψ , Θ , ψ' , θ' at the channel walls as in [8, 37]. These boundary conditions can be verified to require that the temperature difference between the channel walls remains fixed. In this work we have chosen to isolate the primarily barotropic nature of jet formation and equilibration dynamics by taking this temperature difference to be zero. Simulations including baroclinic influences arising from temperature gradients below the threshold required for baroclinic instability, as is appropriate for Saturn, show small changes in the results.

The corresponding quasi-linear system (QL) is obtained by substituting for the perturbation-perturbation interactions in (4) a state independent and temporally delta correlated stochastic excitation together with sufficient added diffusive dissipation to obtain an approximately energy conserving closure [38–40]. Under these assumptions the QL perturbation equations in matrix form for the Fourier components of the barotropic and baroclinic streamfunction are:

$$\frac{d\psi_k}{dt} = \mathbf{A}_k^{\psi\psi} \psi_k + \mathbf{A}_k^{\psi\theta} \theta_k + \sqrt{\varepsilon} \Delta_k^{-1} \mathbf{F}_k \xi^\psi(t), \quad (6a)$$

$$\frac{d\theta_k}{dt} = \mathbf{A}_k^{\theta\psi} \psi_k + \mathbf{A}_k^{\theta\theta} \theta_k + \sqrt{\varepsilon} \Delta_{k\lambda}^{-1} \mathbf{F}_k \xi^\theta(t). \quad (6b)$$

The variables in (6) are the Fourier components of the perturbations fields given by $\psi' = \text{Re}(\sum_k \psi_k e^{ikx})$ and $\theta' = \text{Re}(\sum_k \theta_k e^{ikx})$. The states ψ_k and θ_k are column vectors with entries the complex value of the barotropic and baroclinic streamfunction at the collocation points in y . The excitations, which represent both the explicit excitation and the stochastic parameterization of the perturbation-perturbation interactions in the perturbation equations, is similarly expanded so that the excitation at collocation point y_i is $f_\psi(x, y_i, t) = \text{Re}(\sum_k \sum_j F_{k,ij} \xi_j^\psi(t) e^{ikx})$, $f_\theta(x, y_i, t) = \text{Re}(\sum_k \sum_j F_{k,ij} \xi_j^\theta(t) e^{ikx})$, with ξ^ψ and ξ^θ independent temporally delta correlated vector complex stochastic processes of zero mean satisfying:

$$\begin{aligned} \langle \xi^\psi(t_1) \xi^{\psi\dagger}(t_2) \rangle &= \langle \xi^\theta(t_1) \xi^{\theta\dagger}(t_2) \rangle \\ &= \delta(t_1 - t_2) \mathbf{I}, \quad (7a) \end{aligned}$$

$$\langle \xi^\psi(t_1) \xi^{\theta\dagger}(t_2) \rangle = 0, \quad (7b)$$

in which $\langle \bullet \rangle$ denotes the ensemble average over forcing realizations, \mathbf{I} the identity matrix and \dagger the Hermitian transpose. This excitation is homogeneous in the zonal

direction and identical in each layer. In order to ensure homogeneity in y the latitudinal structure matrices F_k are chosen so that their (i, j) entry is a function of $|y_i - y_j|$. The operators A_k have components:

$$A_k(\mathcal{U}) = \begin{pmatrix} A_k^{\psi\psi} & A_k^{\psi\theta} \\ A_k^{\theta\psi} & A_k^{\theta\theta} \end{pmatrix} \quad (8)$$

with entries:

$$A_k^{\psi\psi} = \Delta_k^{-1} [-ikU\Delta_k - ik(\beta - D^2U)] - r_p + \nu\Delta_k, \quad (9a)$$

$$A_k^{\psi\theta} = \Delta_k^{-1} [-ikH\Delta_k + ikD^2H], \quad (9b)$$

$$A_k^{\theta\psi} = \Delta_{k\lambda}^{-1} [-ikH\Delta_k + ikD_\lambda^2H], \quad (9c)$$

$$A_k^{\theta\theta} = \Delta_{k\lambda}^{-1} [-ikU\Delta_{k\lambda} - ik(\beta - D^2U) + \nu\Delta_k\Delta_k] - r_p, \quad (9d)$$

in which $\Delta_k \stackrel{\text{def}}{=} D^2 - k^2$, $\Delta_{k\lambda} \stackrel{\text{def}}{=} \Delta_k - 2\lambda^2$. Diffusion is included in the perturbation dynamics for numerical stability and its coefficient, ν , is set equal to the square of the grid interval.

The corresponding S3T statistical state dynamics system expresses the dynamics of an equivalently infinite ensemble of realization of the QL equations (6), with each ensemble member sharing the same mean \mathcal{U} while being excited by an independent noise process. This ensemble of perturbation equations is coupled to the mean equation (4) through the ensemble mean vorticity fluxes: $\langle \overline{vq_\psi} \rangle$ and $\langle \overline{vq_\theta} \rangle$. Identifying the ensemble mean with the zonal mean is made by appeal to the ergodic hypothesis (cf. [25]). The appropriate perturbation variable for this SSD is the covariance matrix, which is the second cumulant of the statistical dynamics. The covariance for the wavenumber k zonal Fourier component is defined as:

$$C_k = \begin{pmatrix} C_k^{\psi\psi} & C_k^{\psi\theta} \\ C_k^{\theta\psi} & C_k^{\theta\theta} \end{pmatrix}, \quad (10)$$

where $C_k^{\psi\psi} = \langle \psi_k \psi_k^\dagger \rangle$, $C_k^{\psi\theta} = \langle \psi_k \theta_k^\dagger \rangle$, $C_k^{\theta\theta} = \langle \theta_k \theta_k^\dagger \rangle$. The ensemble mean vorticity fluxes in (4) are expressed in terms of the SSD perturbation variable C_k as:

$$\begin{aligned} \langle \overline{vq_\psi} \rangle &\stackrel{\text{def}}{=} \sum_k \langle \overline{vq_\psi} \rangle_k \\ &= \sum_k \frac{k}{2} \text{diag} \left[\Im \left(D^2 C_k^{\psi\psi} + D^2 C_k^{\theta\theta} \right) \right], \end{aligned} \quad (11a)$$

$$\begin{aligned} \langle \overline{vq_\theta} \rangle &\stackrel{\text{def}}{=} \sum_k \langle \overline{vq_\theta} \rangle_k \\ &= \sum_k \frac{k}{2} \text{diag} \left[\Im \left(D_\lambda^2 C_k^{\psi\theta} + D^2 C_k^{\psi\theta} \right) \right], \end{aligned} \quad (11b)$$

with the diag operator selecting the diagonal elements of a matrix and \Im denoting the imaginary part. The fluxes

are evaluated at each time from C_k as it evolves according to the Lyapunov equation:

$$\frac{dC_k}{dt} = A_k(\mathcal{U}) C_k + C_k A_k^\dagger(\mathcal{U}) + \varepsilon Q_k, \quad (12)$$

with Q_k the covariance of the stochastic excitation (cf. [25, 35]). The covariances Q_k are normalized so that for each k an equal amount of energy is injected per unit time so that the excitation rate is controlled by the parameter ε . The normalization is chosen so that $\varepsilon = 1$ corresponds to injection of $10^{-4} \text{ W m}^{-2} \text{ kg}^{-1}$. Note that because the excitation has been assumed temporally delta-correlated this energy injection rate is independent of the state of the system.

We consider two types of excitation. When both layers are independently excited (this case is indicated with $E_{1,2}$) the covariance of the excitation is:

$$Q_k = \begin{pmatrix} \Delta_k^{-1} F_k F_k^\dagger \Delta_k^{-1\dagger} & 0 \\ 0 & \Delta_{k\lambda}^{-1} F_k F_k^\dagger \Delta_{k\lambda}^{-1\dagger} \end{pmatrix}. \quad (13)$$

When only the top layer is excited (case indicated E_1) the covariance is given by:

$$Q_k = \begin{pmatrix} \Delta_k^{-1} F_k F_k^\dagger \Delta_k^{-1\dagger} & \Delta_k^{-1} F_k F_k^\dagger \Delta_k^{-1\dagger} \\ \Delta_k^{-1} F_k F_k^\dagger \Delta_k^{-1\dagger} & \Delta_k^{-1} F_k F_k^\dagger \Delta_k^{-1\dagger} \end{pmatrix}. \quad (14)$$

The S3T dynamics for the evolution of the first two cumulants of the flow takes the form:

$$\frac{dU}{dt} = \sum_k \langle \overline{vq_\psi} \rangle_k - r_m U, \quad (15a)$$

$$\frac{dH}{dt} = D_\lambda^{-2} D^2 \sum_k \langle \overline{vq_\theta} \rangle_k - r_m H, \quad (15b)$$

$$\frac{dC_k}{dt} = A_k(\mathcal{U}) C_k + C_k A_k^\dagger(\mathcal{U}) + \varepsilon Q_k, \quad (15c)$$

with the vorticity fluxes given in terms of the C_k in (11) and the operators A_k defined in (9).

The S3T system represents the second cumulant with an infinite perturbation ensemble and it is therefore autonomous and as a result has the very useful property for theoretical investigation of providing exact stationary fixed point solutions for statistical equilibrium states. Because the excitation is spatially homogeneous the zero mean flow, $U = H = 0$, together with the perturbation field, C_k^e , satisfying the corresponding steady state Lyapunov equations, is an equilibrium solution for any ε (15c) (for the explicit expression of the equilibrium covariance see [41]). However, this homogeneous equilibrium state is unstable in the S3T system for ε greater than a critical ε_c . This critical value of excitation rate resulting in unstable jet growth in the S3T system can be found by analyzing the stability of perturbations from

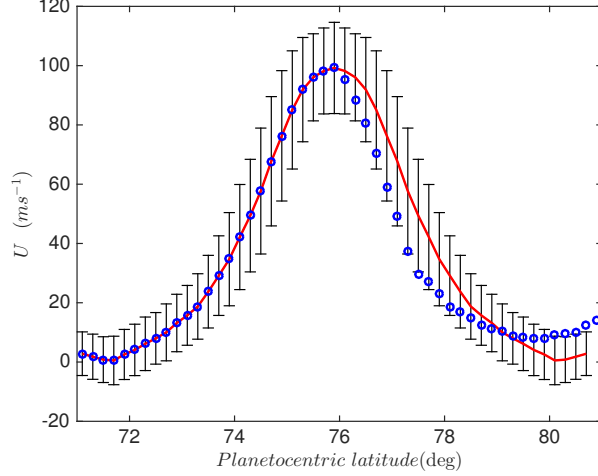


FIG. 1: Observed NPJ velocity (circles) from [18]. The observed jet has been symmetrized by reflecting its southern flank about the jet maximum (solid line with one standard deviation error bounds).

this equilibrium state of (15) (cf. [35]). As ε is increased beyond ε_c this instability results in a bifurcation in which finite amplitude jet equilibrium solutions, $\mathcal{U}^e = [U^e, H^e]$, emerge with appropriately configured covariances \mathbf{C}_k^e that are stable for a range of ε and satisfy the steady state equations:

$$\sum_k \langle \bar{v} \bar{q}_\psi \rangle_k = r_m U^e, \quad D^2 \sum_k \langle \bar{v} \bar{q}_\theta \rangle_k = r_m D_\lambda^2 H^e, \quad (16a)$$

$$\mathbf{A}_k(\mathcal{U}^e) \mathbf{C}_k^e + \mathbf{C}_k^e \mathbf{A}_k^\dagger(\mathcal{U}^e) = -\varepsilon \mathbf{Q}_k, \quad (16b)$$

Remarkably, these equilibria exist even for $r_m = 0$. This limit is especially useful for theoretical investigation because the associated equilibria have a universal form: when $r_m = 0$ it follows from the linearity of (16b) that if \mathcal{U}^e , \mathbf{C}_k^e (for the excited k) is an equilibrium solution for $\varepsilon = 1$ then the same \mathcal{U}^e is an equilibrium solution with $\varepsilon \mathbf{C}_k^e$ for any ε . For large enough ε , however, this equilibrium solution may itself become S3T unstable.

PARAMETERS

The first 56 zonal wavenumbers, $k_x = 2\pi n/L_x$ with $n = 1, \dots, 56$, are excited in the perturbation dynamics. These are referred to alternatively as global wavenumbers or waves $n = 1, \dots, 56$. The simulations use 64 grid points in y with convergence verified by doubling this resolution. The stochastic excitation has Gaussian structure in y with \mathbf{F}_k chosen so that the (i, j) element of the excitation is proportional to $\exp(-(y_i - y_j)^2/\delta^2)$, with $\delta = 1$. Recall that the associated excitation covariances in the S3T dynamics, \mathbf{Q}_k , are normalized so that each wavenumber provides the same energy injection rate

and that with $\varepsilon = 1$ the total energy injection rate over all wavenumbers is dimensionally 10^{-4} Wkg^{-1} . We have chosen for modeling the NPJ a doubly periodic channel with parameter values: $L_y = 10^4 \text{ km}$, $L_x = 8 \times 10^4 \text{ km}$, $\beta_{\text{sat}}(74^\circ) = 1.6 \times 10^{-12} \text{ m}^{-1}\text{s}^{-1}$, $\lambda = 1/10^3 \text{ km}^{-1}$, perturbation damping $r_p = 0.2 \text{ day}^{-1}$ and excitation $\varepsilon = 1$.

UNIVERSAL STRUCTURE AND AMPLITUDE SCALING OF WEAKLY DAMPED TURBULENT JETS

The velocity structure of the NPJ is asymmetric presumably because the jet is influenced by encroachment of the polar vortex flow on its north side (cf. Fig. 1). For simplicity we model a symmetric channel and consistently choose to compare our results with a symmetrized jet obtained by reflecting the southern half of the observed jet structure about the jet maximum. This symmetrized jet together with one standard deviation error bounds as tabulated in [18] is shown in Fig. 1.

We anticipate that the jet dynamics will be in the small jet damping regime in which the exact value of r_m is irrelevant and can be taken to vanish. With the remaining parameter value given above we find that a barotropic jet with a single maximum in zonal velocity arises as an unstable S3T eigenmode. Because the jet and the large scale waves are barotropic, the Rossby radius is expected to have little affect on the dynamics of these scales, which we have verified. We wish to study the influence on the S3T jet and associated perturbation covariance of the perturbation damping rate, r_p , the amplitude of the excitation, ε , and β . In the limit of small r_m the time required to reach equilibrium depends on r_m but the final equilibrium jet structure depends to a good approxima-

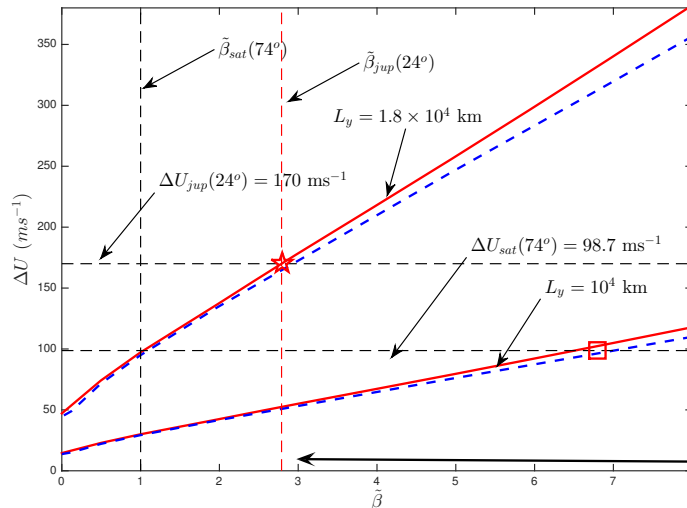


FIG. 2: S3T equilibrium jet amplitude, ΔU , as a function of $\tilde{\beta} = \beta/\beta_{\text{sat}}(74^\circ)$ in the low jet damping regime. ΔU is the difference between the maximum and the minimum jet velocities. Indicated are values of $\tilde{\beta}$ for Saturn's NPJ ($L_y = 10^4$ km) and for Jupiter's 24° N jet ($L_y = 1.8 \times 10^4$ km). The equilibria for this case in which equal excitation has been imposed in both layers are barotropic and continuous lines indicate these equilibria for $r_m = 0$. Dashed lines showing these equilibria for $r_m = 0.001 \text{ day}^{-1}$ differ little indicating the validity of the $r_m = 0$ asymptotic. The dependence on ε and r_p of these asymptotic jets is also very weak and is not shown. The asymptotic scaling of the jet amplitude ΔU with βL_y^2 is nearly perfect for $\tilde{\beta} > 3$ (marked with an arrow). Also indicated are the planetary values of $\tilde{\beta}_{\text{sat}}(74^\circ)$, $\tilde{\beta}_{\text{jup}}(24^\circ)$, the observed $\Delta U_{\text{sat}}(74^\circ) = 98.7 \text{ ms}^{-1}$ from [18] and the observed $\Delta U_{\text{jup}}(24^\circ) = 170 \text{ ms}^{-1}$ from [42]. While the observed $\Delta U_{\text{jup}}(24^\circ)$ (star) is consistent with the planetary value of β as predicted by the asymptotic theory, the observed $\Delta U_{\text{sat}}(74^\circ)$ (square) requires $\tilde{\beta} = 6.9$ for consistency.

tion only on the channel width and β . In this regime, the jet amplitude and structure are nearly independent of the excitation rate, ε , and the perturbation damping rate, r_p , while the perturbation energy is to a very good approximation proportional to their ratio ε/r_p . The jet structure obtained in the limit $r_m \rightarrow 0$ is close to the observed structure so we exploit the simplicity of this limit by studying the jet dynamics with zero mean jet damping, $r_m = 0$. Departures from the $r_m = 0$ equilibrium solution resulting from physically relevant nonzero jet damping rates are verified to be small (cf. Fig. 2).

With $r_m = 0$ the equilibrium jet velocity varies approximately linearly with βL_y^2 as shown in Fig. 2 in which the values of β appropriate for Saturn's NPJ and for Jupiter's 24° N jet are indicated. As β increases the equilibrium jet assumes a universal structure the amplitude of which scales with the product of β and the square of the channel size, L_y , as shown in Fig. 3. While Jupiter's 24° N jet corresponds closely with this universal scaling (cf. Fig. 3c), Saturn's NPJ is observed to be substantially stronger at 98.7 m/s than the approximately 30 ms^{-1} (cf. Fig. 2) predicted by the scaling for $\beta_{\text{sat}}(74^\circ) = 1.6 \times 10^{-12} \text{ m}^{-1}\text{s}^{-1}$ and the NPJ channel width of $L_y = 10^4 \text{ km}$. The effective value of β required to obtain correspondence with the scaling is

$$\beta_{\text{eff}} = 6.9\beta_{\text{sat}}(74^\circ)$$

As we will show, the mechanism underlying establishment of these equilibria is associated with sign change of the vorticity gradient in the retrograde jet, which is accompanied by the appearance of a mode. The jet equilibrium is established by a robust feedback regulation arising from interaction between the mean equation and the perturbation covariance equation associated with the appearance of this mode and its strong downgradient momentum flux. The mean jet, which is undamped, grows from an arbitrarily small perturbation in the mean flow at first exponentially under the influence of the up-gradient fluxes induced by shear straining of the short waves. This growth is abruptly terminated by down-gradient fluxes associated with the arising of this highly non-normal nearly neutral mode as the jet vorticity gradient sign change begins to be established (cf. Fig. 4). Extensive experimentation has convinced us that this incipient instability closely constrains the jet amplitude to allow only relatively small vorticity gradient sign changes to occur. Because close regulation of the mean flow by fluxes arising in association with incipient instabilities is so robust it is widely recognized that the large magnitude of the vorticity gradient sign change in the NPJ observations poses a conundrum [18]. Within our model

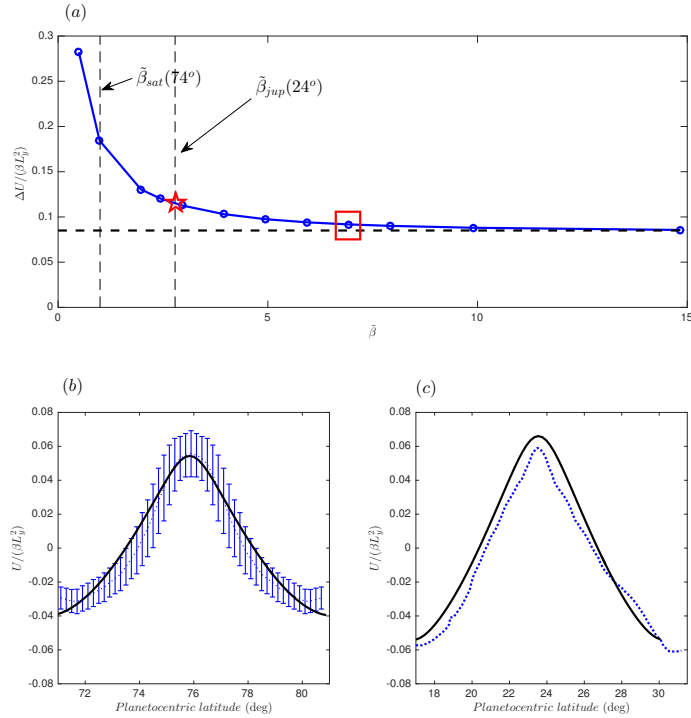


FIG. 3: Universal structure of the S3T equilibrium jets for vanishing jet damping, $r_m = 0$. Panel (a): normalized equilibrium jet amplitude, $\Delta U/(\beta L_y^2)$, as a function of $\tilde{\beta} = \beta/\beta_{sat}(74^\circ)$. For large $\tilde{\beta}$ the S3T equilibrium flows assume an asymptotic structure and amplitude $\Delta U/(\beta L_y^2) \approx 0.085$. Panel (b): the observed NPJ from [18] which has been symmetrized, scaled and had its mean removed (dotted with error bounds) compared to the scaled S3T equilibrium jet for $\tilde{\beta} = 6.9$ (indicated with a square in Panel (a)). Panel (c): the observed Jupiter 24°N jet from [42] which has been similarly symmetrized, scaled and had its mean removed (dotted) compared to the scaled S3T equilibrium jet for $\tilde{\beta} = 2.8$ (indicated with a star in Panel (a)) for channel size $L_y = 1.8 \times 10^4$ km. These barotropic equilibria are obtained with the two layers equally excited with $\varepsilon = 1$ corresponding to energy injection of $10^{-4} \text{ W kg}^{-1}$ and $r_p = 0.2 \text{ day}^{-1}$. This figure confirms that these planetary jets correspond to $r_m = 0$ S3T equilibrium solution and approach the predicted asymptotic structure as $\tilde{\beta}$ increases.

framework this discrepancy between the observed large vorticity gradient sign change in the observations of the upper layer of the NPJ can only be resolved by regarding the observed jet equilibrium as an indirect observation of a larger effective value of β in the unobserved lower layer of the NPJ and in fact the S3T equilibrium jet with an appropriate choice of β , which is $\beta_{eff} = 6.9\beta_{sat}(74^\circ)$, is in close agreement with the observed NPJ jet (cf. Fig. 3b). We wish now to establish the dynamical argument compelling this conclusion.

THE EQUILIBRATION MECHANISM UNDERLYING THE ROBUST SCALING OF WEAKLY DAMPED TURBULENT JETS

We turn now to study in more detail the mechanism underlying the universal scaling of the structure and am-

plitude of weakly damped turbulent jets.

Note that in an undamped jet at equilibrium the perturbation momentum flux divergence vanishes at each latitude, $\overline{vq}(y) = 0$ (cf. $t = 1000$ right panel of Fig. 4). Moreover, this requirement is independent of the stochastic excitation amplitude, ε . As previously mentioned, for a given ε , perhaps from observational constraints, the energy of the perturbation field at equilibrium can be shown to increase inversely with perturbation damping, r_p , to a good approximation. These considerations imply invariant structure at equilibrium in the small r_m limit for both the jet (cf. Fig. 3) and the perturbation turbulence component with only the amplitude of the perturbation turbulence component varying and that variation being as the ratio of excitation to damping, ε/r_p .

In addition to its anomalous strength given the small planetary value of β available to stabilize it, the NPJ is also remarkable for supporting a prominent wavenum-

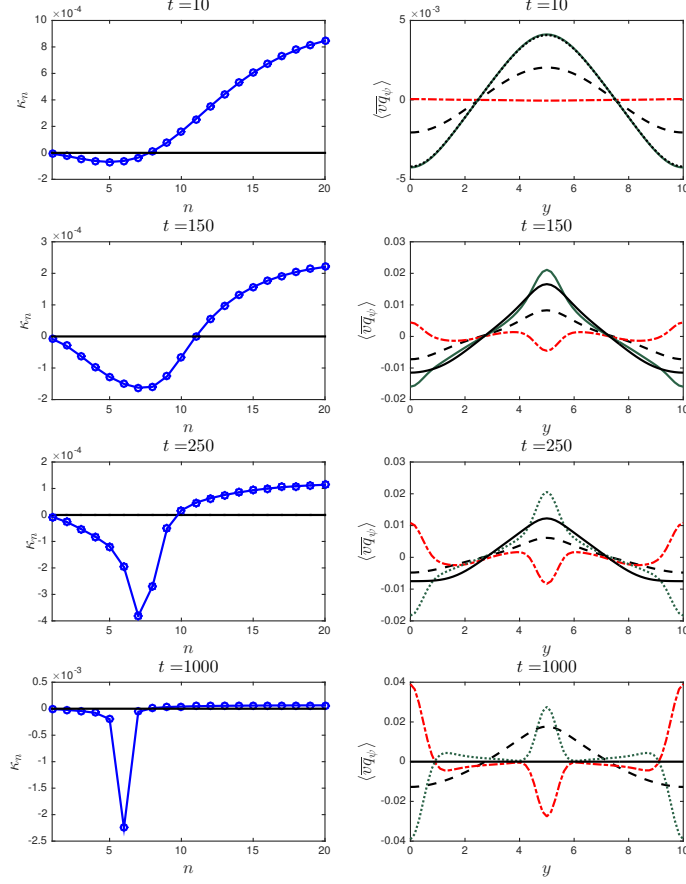


FIG. 4: Left panels: normalized rate of energy input to the jet by each wave n , $\kappa_n = \int_0^{L_y} dy U \langle \overline{vq_\psi} \rangle_n / \int_0^{L_y} dy U^2 / 2$ (day^{-1}), for times $t = 10, 150, 250, 1000$ as the S3T equilibrium is established starting from a small random initial jet structure. Right panels: the latitudinal distribution of the vorticity flux $\langle \overline{vq_\psi} \rangle$ (solid) (units: $11.57 \text{ ms}^{-1} \text{ day}^{-1}$), the vorticity flux $\langle \overline{vq_\psi} \rangle_+ = \sum_{n=12}^{56} \langle \overline{vq_\psi} \rangle_n$ from zonal waves $n \geq 12$ (dashed line), and the vorticity flux $\langle \overline{vq_\psi} \rangle_- = \sum_{n=1}^{11} \langle \overline{vq_\psi} \rangle_n$ from zonal waves $n < 12$ (dotted line). The structure of the zonal velocity at the corresponding time is indicated with a dashed line (amplitude arbitrary chosen to fit the graph). Vorticity fluxes $\langle \overline{vq_\psi} \rangle_+$ are upgradient and are responsible for forming and maintaining the jet, vorticity fluxes $\langle \overline{vq_\psi} \rangle_-$ are downgradient opposing the jet and these are responsible for the jet equilibration. The S3T equilibrium is attained by $t = 1000$ so that consistently $\langle \overline{vq_\psi} \rangle(y) = 0$. Energy loss from the jet at equilibrium is concentrated at $n = 6$ and this energy loss is primarily balanced by energy input due to waves with $n \geq 8$. Parameters: $L_y = 10^4 \text{ km}$, $L_x = 8 \times 10^4 \text{ km}$, $\varepsilon = 1$ corresponding to equal energy injection in both layers of 10^{-4} Wkg^{-1} , $r_m = 0$, $r_p = 0.2 \text{ day}^{-1}$ and $\tilde{\beta} = 6.9$.

ber six perturbation with the amplitude required to distort the jet into a distinct hexagonal shape. S3T equilibria comprise both the structure of the mean jet and the perturbation covariance from which information on perturbation structure can be determined. A temporal sequence showing establishment of the equilibrium structure of the NPJ starting from a random initial condition and assuming the inferred $\tilde{\beta} = 6.9$ is shown in Fig. 4. As is generally found, the upgradient fluxes are produced by

the short waves [43, 44], which in the case of the NPJ means waves with $n > 12$. Conversely, downgradient fluxes are produced by the long waves with $n \leq 8$. The upgradient fluxes are associated with shear straining of the short waves which is a universal mechanism resulting in a negative viscosity in that it produces upgradient momentum flux proportional to the velocity gradient [45] as is observed in the atmospheres of both Jupiter and Saturn [21–23]. This shear straining mechanism accelerates

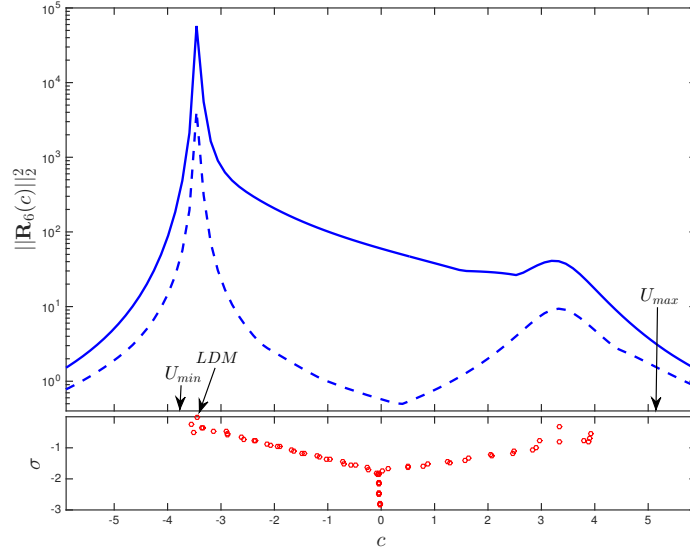


FIG. 5: Top panel: the square of the energy norm of the resolvent for $n = 6$, $\|\mathbf{R}_6(c)\|_2^2$, (solid) as a function of phase speed, c , indicating the maximum energy amplification over all latitudinal structures $f(y)$ for unit energy harmonic forcing of the form $f(y) e^{ik(x-ct)}$ with $k = 2\pi n/L_x$. Also shown is the square of the energy norm of the equivalent normal resolvent which would obtain if the eigenfunctions of \mathbf{A}_k were orthogonal (dashed). In the bottom panel is shown the growth rate, σ , and phase speed, c , of the modes of \mathbf{A}_k for $n = 6$ (circles). The dominant response arises in association with the nearly neutral least damped mode (indicated LDM). The equivalent normal response is substantially smaller than the actual response indicating that non-normal interactions dominate the energetics at all phase speeds and most importantly at the phase speed of the LDM where the maximum interaction occurs.

Quantities are non-dimensional and parameters as in Fig. 4.

both the prograde and retrograde jets. When the homogeneous turbulence is perturbed by a random mean jet these upgradient fluxes immediately cause the jet to grow in the form of the most unstable S3T eigenmode (cf. time $t = 10$ in Fig. 4) [30, 35]. As the jet amplitude increases the retrograde jet progressively exceeds the speed of the slower retrograde Rossby modes and these sequentially obtain critical layers inside the retrograde jet [46]. Approach to and attainment of a critical layer by these modes is accompanied by increasing modal as well as non-normal energetic interaction with the jet which produces increasing downgradient fluxes opposing the growth of the S3T jet eigenmode so as to eventually establish a nonlinear equilibrium. As neutral stability is approached with increasing jet amplitude these fluxes come into balance establishing by time $t = 1000$ the stable fixed point equilibrium turbulent jet structure and associated perturbation covariance that together constitute a complete solution for the turbulent state at second order as shown in Fig. 4.

Further insight into the dynamics can be obtained by calculating the eigenvalues and the resolvent of the perturbation dynamics operator $\mathbf{A}_k(\mathbf{U})$ as the jet structure \mathbf{U} evolves toward equilibrium. The eigenvalues reveal the

approach of the retrograde modes' phase speeds to the speed of the retrograde jet and the associated decrease in mode damping rate which is indicative of energetic interaction with the jet and diagnostic of downgradient momentum flux by the mode. The resolvent of $\mathbf{A}_k(\mathbf{U})$ provides more information by revealing the response of the dynamics to the turbulent excitation at each mode phase speed, c . The resolvent is obtained by solving the Fourier transform of the dynamics (cf. [47]):

$$\mathbf{R}_n(c) = -(ikc\mathbf{I} + \mathbf{A}_k)^{-1}, \quad (17)$$

in which \mathbf{I} is the identity matrix. The square norm of the resolvent of $\mathbf{A}_k(\mathbf{U})$, which is the energy spectrum as a function of phase speed for temporally and spatially delta correlated excitation, is shown together with the spectrum of the modes of $\mathbf{A}_k(\mathbf{U})$ for the equilibrium jet structure, \mathbf{U} , in Fig. 5. There is a dominant nearly neutral Rossby mode with wavenumber six that is responsible for most of the downgradient momentum flux balancing the upgradient shear straining fluxes from the short waves (cf. Fig. 4 at $t = 1000$). This wave dominates the response of the dynamics to perturbation when the jet is equilibrated as can be inferred from the resolvent. This dominance of wavenumber six in the perturbation

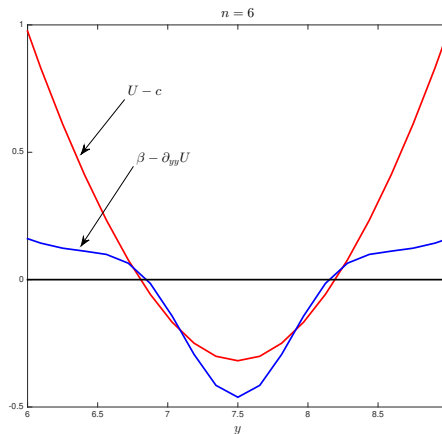


FIG. 6: Detail near the minimum velocity of the retrograde S3T jet at equilibrium with $\tilde{\beta} = 6.9$ showing the critical layer of the LDM, $U(y) - c$, where c is the phase speed of the nearly neutral LDM of \mathbf{A}_k for $n = 6$. Also shown is the jet vorticity gradient, $\beta - \partial_{yy}U$, as a function of y . Note that the perturbation/mean interaction has stabilized the LDM by nearly eliminating the vorticity gradient in the vicinity of this mode's critical layer while leaving a small change in vorticity gradient sign between the mode's critical layers. Such changes in sign of the vorticity gradient are a commonly observed feature of turbulent jets in planetary atmospheres. Quantities are non-dimensional and parameters as in Fig. 4.

variance extends over a wide range in β and therefore in equilibrium jet amplitude as shown in Fig. 2. Note that the phase speed of this mode has been incorporated into the retrograde jet but that this mode remains stable consistent with finiteness of the perturbation variance. The strong \overline{vq} fluxes associated with the maintenance of this mode have forced the gradient of the mean vorticity in the vicinity of its critical layer nearly to zero as shown in Fig. 6. This nonlinear interaction provides an example of the mechanisms at play in the complex feedback stabilization process operating between the first and second cumulants in the S3T dynamics that results in establishment of the equilibrium statistical state. It is useful to regard this interaction as a nonlinear regulator that continuously adjusts the mean flow to a state that is in neutral equilibrium with the perturbation dynamics by enforcing vanishing of the mean vorticity gradient at the critical layers of the dominant perturbation modes in the retrograde jet. This consideration explains why strongly excited jet equilibria in planetary atmospheres commonly exhibit easily observable changes in sign of the mean vorticity gradient without incurring instability: shear straining of the small turbulence components drives both the prograde and retrograde jets strongly producing the sign change while the regulator need only equilibrate any incipient modal instability by enforcing vanishing of the gradient at the mode critical layer while leaving a substantial vorticity sign change between the critical layers in the jet profile. It is important to appreciate the crucial role of active feedback regulation continually operating between the first and second cumulants in the SSD

in maintaining the stability of this turbulent equilibrium jet/wave/turbulence state. If one were simply to postulate a jet profile very much like the observed it would be extremely unlikely to have by chance the vanishing gradient of vorticity precisely at the critical layers of the mode required for stability of the jet structure. Viewed another way, the existence of strong jet equilibria with the structure seen in planetary atmospheres requires that an active feedback regulation be operating to maintain their stability. Note that the mechanism of vorticity mixing in the retrograde jets could not result in a negative vorticity maximum as is seen in both observations and our simulations.

While it is tempting to regard the downgradient momentum fluxes arising from the dominant mode itself as being primarily responsible for opposing the upgradient fluxes by the small waves, the resolvent tells a different story. Shown in Fig. 5 is both the response of the jet dynamics to perturbation as a function of phase speed and the response that would be produced by the modes assuming they were independent; that is, assuming the modes to be orthogonal in energy. This so called equivalent normal response reveals that the energetics and therefore the fluxes associated with the LDM at $n = 6$ are being produced by non-normal interaction among the modes rather than by the $n = 6$ mode by itself. In fact it is generally the case in non-normal systems that transient growth of the adjoint of a mode is responsible for establishing a mode's equilibrium amplitude when it is excited stochastically rather than growth of the mode itself [47].

Because of its dominance the structure of the $n = 6$

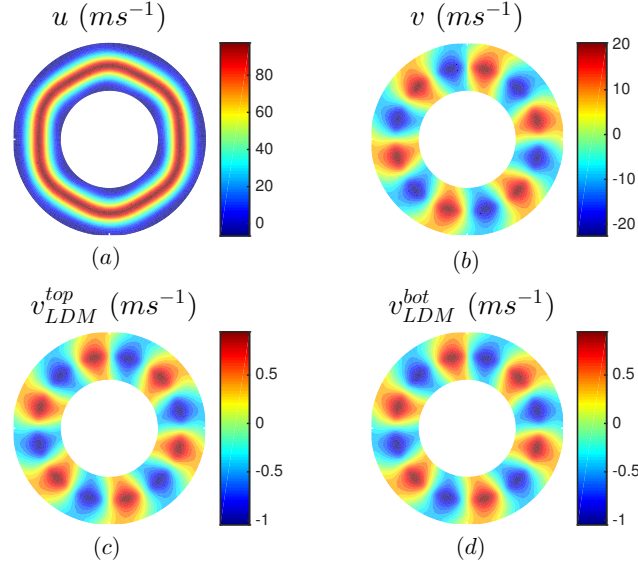


FIG. 7: The predicted NPJ velocity structure in a polar rendering of the S3T model channel in which the radial distance from the pole has been taken to be proportional to the channel coordinate y . Upper left panel: contours of the zonal velocity obtained by adding the S3T equilibrium zonal mean velocity and the velocity of the first POD mode obtained from eigenanalysis of the equilibrium perturbation covariance at zonal wavenumber $n = 6$. This mode accounts for 99.5% of the perturbation energy at this wavenumber. The amplitude of the wave is obtained from the associated eigenvalue of the equilibrium perturbation covariance. The jet is barotropic as is the $n = 6$ wave. Upper right panel: contours of the meridional velocity of the first POD of the perturbation covariance at zonal wavenumber $n = 6$. Bottom panels: The structure in the top and bottom layer of the least damped mode (LDM) of A_k at $n = 6$ (cf. Fig. 5). It is clear from this comparison that the LDM is barotropic and the POD has the structure of this mode. Parameters are as in Fig. 4.

perturbation can be obtained as the first eigenmode of the perturbation covariance (referred to variously as the leading proper orthogonal decomposition (POD) or empirical orthogonal function (EOF) mode). This structure is shown in Fig. 7b and its superposition on the jet with amplitude obtained as the RMS of its variance as obtained from the associated POD eigenmode is shown in Fig. 7a. Consistent with the resolvent diagnostic discussed above, this mode has nearly the same structure as the least damped mode of the linear perturbation dynamics shown in Fig. 7c,d, and both have barotropic structure. The amplitude of the wave six mode is proportional to ε/r_p and we have chosen physically defensible values for these parameters $\varepsilon = 1$ and $r_p = 0.2 \text{ day}^{-1}$ corresponding to excitation of 10^{-4} Wkg^{-1} . However, other combinations of ε and r_p with $\varepsilon/r_p = 5$ lead to equilibria very close to those obtained with these parameter values.

THE DEEP STABLE LAYER NPJ MODEL

Our study of the dynamical consequences for jet formation and equilibration of varying the planetary value of β reported above has the advantage of allowing the

underlying mechanisms and the associated scaling to be understood in a simple context. However, the physical mechanism by which an effective value of β differing from the planetary value enters the dynamics of the NPJ is likely to be a poleward sloping surface of concentrated downward increase in static stability underlying the deep jet which would induce the dynamic analogue of a topographic β effect in the lower layer. This equivalent sloping lower boundary could be associated with constitutive, convective and/or dynamical processes analogous to those which are responsible for maintaining the Earth's tropopause but lacking observation it is not possible to identify the specific processes responsible.

A topographic β effect results in different values of effective β in the two layers rather than the same value in both as was appropriate when varying the planetary value of β in the theoretical development above. In the top layer the zonal mean potential vorticity gradient (PV gradient) is $Q_{1y} = \beta_{sat} - \partial_{yy}U_1 + \lambda^2(U_1 - U_2)$, with β_{sat} designated the planetary value of β , and in the bottom layer it is $Q_{2y} = \beta_{sat} + \beta_h - \partial_{yy}U_2 - \lambda^2(U_1 - U_2)$, in which the planetary value of β has been designated β_{sat} and the topographic value β_h . The equations (1) are modified as follows:

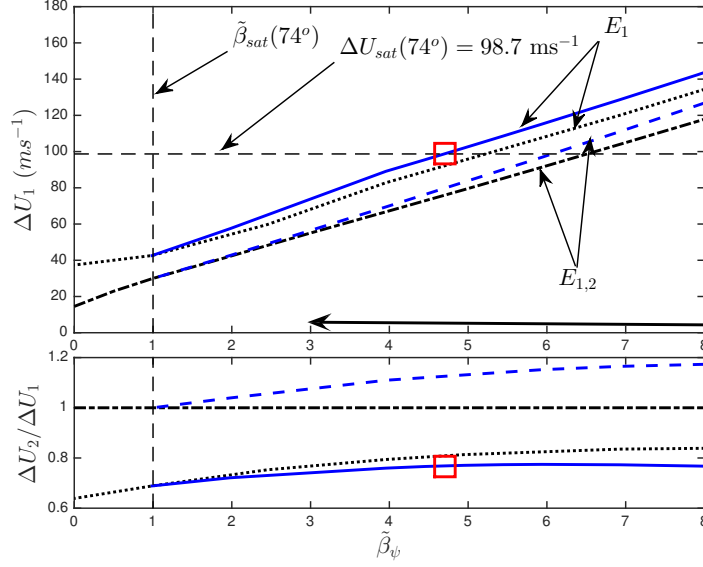


FIG. 8: Top panel: S3T equilibrium jet amplitude, ΔU , as a function of the normalized barotropic β component $\tilde{\beta}_\psi = \beta_\psi / \beta_{sat}(74^\circ)$ for Saturn's NPJ ($L_y = 10^4$ km). ΔU_1 is the difference between the maximum and the minimum jet velocities of the top layer. Lines $E_{1,2}$ indicate equilibria obtained when both layers are equally excited, lines E_1 indicate equilibria obtained when only the top layer is excited. The solid and dashed lines are equilibria with bottom layer $\beta_2 = 2\beta_\psi - \beta_{sat}$ and top layer $\beta_1 = \beta_{sat}$. The dash-dot and dotted lines indicate equilibria in which both layers have the same β_ψ , as in Fig. 2. Also indicated are the planetary values of $\tilde{\beta}_{sat}(74^\circ)$ and the observed $\Delta U_{sat}(74^\circ) = 98.7 \text{ ms}^{-1}$ from [18]; boxes indicate the point consistent with the NPJ observations. The arrow indicates the range of β_ψ for which the perturbation energy is concentrated in a single nearly neutral wave with phase speed near that of the jet minimum, which for the NPJ channel corresponds to $n = 6$. Scaling of ΔU with βL_y^2 is highly accurate in this region. Parameters: $r_m = 0$, $\varepsilon = 1 \text{ W kg}^{-1}$, $L_R = 10^3 \text{ km}$, $r_p = 0.2 \text{ day}^{-1}$. Bottom panel: The resulting baroclinicity of the equilibria, measured as the ratio of $\Delta U_2 / \Delta U_1$ in each layer. Barotropic flows, such as occur when the excitation and β are the same in both layers (cases $E_{1,2}$) have $\Delta U_2 / \Delta U_1 = 1$ (dash-dot line). In all other cases the equilibria are slightly baroclinic. When the upper layer alone is excited (E_1 case in Fig. 8) the jet in the top layer is stronger than the jet in the bottom layer (solid and dotted lines). If both layers are excited and the value of β in the bottom layer is greater than that in the top layer, the bottom jet is the stronger (dashed line).

$$\begin{aligned} \partial_t \Delta \psi + J(\psi, \Delta \psi) + J(\theta, \Delta \theta) + \beta_\psi \psi_x + \\ + \beta_\theta \theta_x = -r \Delta \psi + \sqrt{\varepsilon} f_\psi, \end{aligned} \quad (18a)$$

$$\begin{aligned} \partial_t \Delta \lambda \theta + J(\psi, \Delta \lambda \theta) + J(\theta, \Delta \psi) + \beta_\psi \theta_x + \\ + \beta_\theta \psi_x = -r \Delta \lambda \theta + \sqrt{\varepsilon} f_\theta, \end{aligned} \quad (18b)$$

with the barotropic, β_ψ , and baroclinic, β_θ , defined as:

$$\beta_\psi = \beta_{sat} + \frac{\beta_h}{2}, \quad \beta_\theta = \beta_{sat} - \frac{\beta_h}{2}. \quad (19)$$

The S3T system is modified accordingly. From (18a) we see that the effective value of β seen by waves with primarily barotropic structure such as the planetary wave $n = 6$ that is implicated in the dynamics of the NPJ equilibration is the sum of the planetary value β_{sat} and

half the topographic value, β_h . Results similar to those shown in Fig. 2 for the case of equal β in both layers are shown in Fig. 8 for the case of a topographic β effect with $\beta = \beta_{sat} + \beta_h$ in the bottom layer and $\beta = \beta_{sat}$ in the top layer. Even with equal excitation of the background turbulence in both layers (E_{12} case) both the jet and the waves become slightly baroclinic as seen in Fig. 8 and the jet in this case obtains a higher equilibrium amplitude in the lower layer consistent with the higher effective value of β there. However, when excitation is restricted to the top layer (E_1 case in Fig. 8) the jet in the top layer is the stronger.

Assuming only the top layer is excited a topographic β component in the lower layer of $\beta_h = 8.8\beta_{sat} = 14.4 \times 10^{-12} \text{ m}^{-1} \text{ s}^{-1}$ when combined with the planetary $\beta_{sat}(74^\circ)$ results in consistency with the NPJ upper layer observations as indicated in Fig. 8. With a layer depth equal to one scale height on Saturn, $H = 42.1 \text{ km}$, the

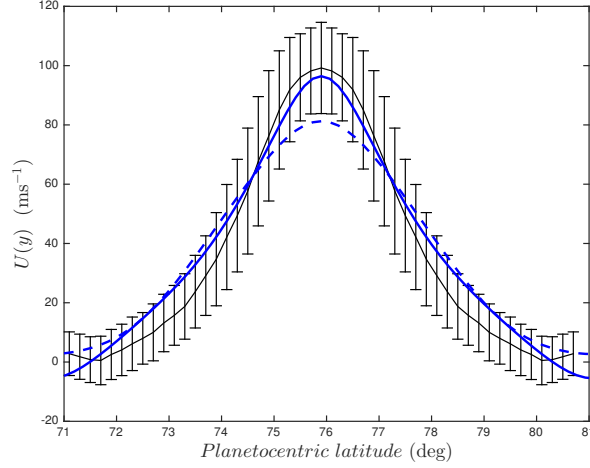


FIG. 9: For the deep stable layer NPJ model: equilibrium jet in the top layer (thick solid line) and bottom layer (thick dashed line). Also shown is the symmetrized observed NPJ from [18] (thin dashed line with one standard deviation error bounds). The S3T equilibria are obtained with stochastic forcing of the top layer, $r_m = 0$, $\lambda = 1$ and $\hat{\beta}_\psi = 4.9$ corresponding to topographic component $\hat{\beta}_h = 8.8$ in the bottom layer. This equilibrium profile is insensitive to variations in ε , r_p and λ .

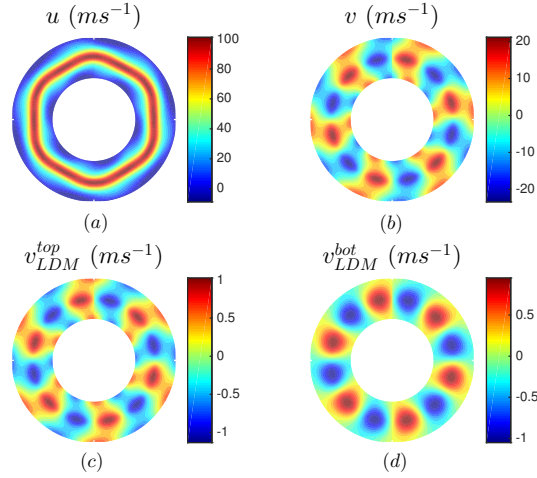


FIG. 10: For the deep stable layer NPJ model shown in Fig. 9: NPJ structure in a polar rendering of the channel. Upper left panel: contours of the zonal velocity as obtained by adding to the S3T equilibrium zonal mean velocity the velocity of the first POD of the equilibrium perturbation covariance at zonal wavenumber $n = 6$ which accounts for 99.7% of the perturbation energy at this wavenumber. The amplitude of the wave is obtained from the associated eigenvalue of the equilibrium covariance. The jet and the $n = 6$ wave are slightly baroclinic. Upper right panel: contours of the meridional velocity of the first POD of the perturbation covariance at zonal wavenumber $n = 6$. Bottom panels: The structure of the least damped mode (LDM) of \mathbf{A}_k for $n = 6$ (indicated in Fig. 11) in the top and bottom layer (left and right panels respectively). The POD has the structure of this mode and both are slightly baroclinic. For $\varepsilon = 0.7$, other parameters as in Fig. 9.

required lower layer slope is

$$h_y = \frac{\beta_h H}{f} = \frac{(14.4 \times 10^{-12} \text{ m}^{-1} \text{ s}^{-1}) \times (42.1 \times 10^3 \text{ m})}{3.1 \times 10^{-4} \text{ s}^{-1}} = 2 \times 10^{-3} ,$$

implying a density surface dynamically equivalent to the bottom boundary sloping downward toward the pole over the channel width of 10000 km from 74.5 km to 93.9 km (measured from the top boundary). We remark that the prominent 24° N jet of Jupiter conforms with the lightly

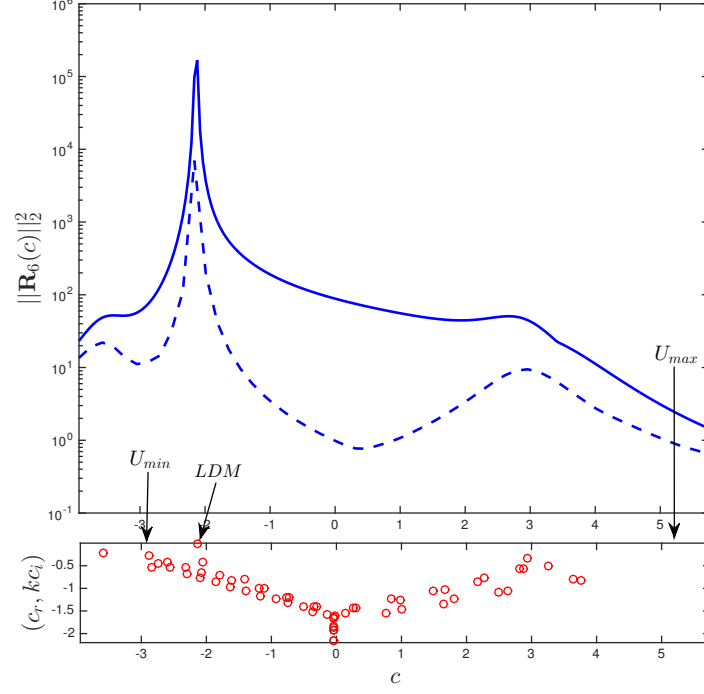


FIG. 11: For the deep stable layer NPJ model equilibrium shown in Fig. 9: in the top panel is shown the square of the energy norm of the resolvent for wave $n = 6$, $\|\mathbf{R}_6(c)\|_2^2$ (solid), together with the equivalent normal response (dashed) as a function of phase speed, c . The dominant response arises from the nearly neutral least damped mode (indicated LDM) with $c = -2.14$ and critical layer inside the retrograde jet. Note the secondary peak caused by the non-normal excitation of the mode with $c = 2.93$ and critical layer inside the prograde jet, as shown in Fig. 13. In the bottom panel is shown the growth rate, σ , and phase speed, c , of the modes of \mathbf{A}_k for $n = 6$ (circles). The equivalent normal response is substantially smaller than the actual response indicating that non-normal interactions dominate the energetics at all phase speeds and most importantly at the phase speed of the LDM where the maximum interaction occurs. There is a secondary peak in the resolvent near $c = 3.5$ associated with the vorticity sign change in the prograde jet but the associated modes are not significant in giving rise to the fluxes responsible for equilibrating the jet. Quantities are non-dimensional and parameters as in Fig. 9.

damped jet scaling using the planetary value of $\beta_{jup}(24^\circ)$, as shown in Fig. 3 which result verifies previous findings [35]. This suggests that the stable lower layer inferred to underly Saturn's NPJ is peculiar to the anomalous thermal and dynamical conditions observed near Saturn's North Pole.

The S3T jet structure in the upper layer with the parameter values given above, which were chosen to model the NPJ, is shown in Fig. 9. A polar representation of the jet and the associated $n = 6$ wave is shown in Fig. 10. The jet equilibration process is essentially similar to that described in the previous section in which the planetary value of β was varied. As in the previous case, most of the perturbation variance is concentrated in the nearly neutral wave 6 which has a critical layer inside the retrograde jet as can be seen in the resolvent response of the $n = 6$ wave shown in Fig. 11. Again, this

nearly neutral wave with critical layer inside the retrograde jet and with primarily non-normal energetics is in large part responsible for producing the upgradient flux to exactly cancel the downgradient flux produced by the waves $n \geq 8$ resulting in establishment of the turbulent equilibrium. In Fig. 12 is shown three snapshots of the temporal development of the optimal initial condition for exciting the LDM demonstrating the dominance of non-normal dynamics in the establishment of this mode. It is interesting to note that the optimal excitation of this mode, which is its adjoint [47, 48], is initially concentrated in the retrograde jet (cf. Fig. 12). As in the previous example and as is required for neutrality, the PV gradient in both the upper and lower critical layers (Q_{y1} and Q_{y2}) is eliminated, primarily by fluxes arising from the non-normal dynamics, as shown in Fig. 13.

The potential vorticity gradient reversals seen in Fig.

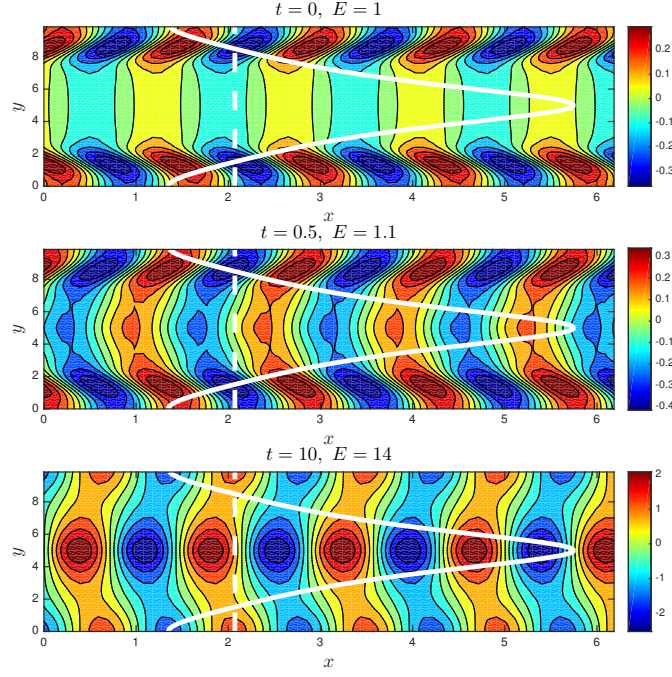


FIG. 12: For the deep stable layer NPJ model equilibrium shown in Fig. 9: establishment of the $n = 6$ LDM by the excitation of its optimal. Shown is the evolution of the optimal as indicated in the top layer streamfunction. Upper panel: the optimal perturbation at $t = 0$ with energy density $E = 1$. Middle panel: the evolved optimal at $t = 0.5$. Bottom panel: the evolved optimal at $t = 10$ at which time it has assumed the structure of the LDM with energy $E = 14$. Contours indicate non-dimensional values of the streamfunction. Also shown is the equilibrium jet (solid), which has been scaled to fit, and the phase speed of the LDM (dashed). While the amplitude of the LDM is concentrated in the prograde jet, its optimal excitation is concentrated near its critical layer in the retrograde jet. The non-normality of the dynamics is indicated by both the large excitation of this stable structure and the substantial structural change during the evolution of the optimal. Parameters as in Fig. 9.

13, which are observed in both Jupiter and Saturn and predicted by the S3T equilibria, provide a probe of the dynamical processes at work in the equilibration of these large amplitude jets. As previously discussed in connection with the planetary β variation example, a strong reversal of Q_{y1} near the minimum of the retrograde jet results from upgradient vorticity fluxes produced by the $n > 8$ waves. The resulting region of potential vorticity gradient reversal is not opposed by the LDM which enforces its own stabilization by eliminating the PV gradient in the vicinity of its critical layers leaving the quite extensive region between these critical layers satisfying the Rayleigh-Kuo necessary condition as shown in Fig. 13. Note that the bottom layer PV gradient has also been eliminated in the region between the critical layers of the $n = 6$ wave. However, in this case with excitation limited to the top layer the shorter waves do not penetrate adequately into the bottom layer to produce sufficiently strong upgradient fluxes to form a PV gradient reversal.

Reversals in PV gradient in the retrograde jet are associated with positive curvature of the mean flow. The

predicted curvature of the mean flow in the top layer is plotted in Fig. 14 against raw observations from [18]. Discussion tends to center on the maximum at the wings of the prograde jet which is responsible for supporting modes associated with the secondary maximum in the resolvent at phase speeds in the prograde jet seen in Fig. 11. However, the modes associated with this prograde jet PV reversal are insignificant in the dynamics. The dynamically significant PV gradient reversal is that between the critical layers of the dominant $n = 6$ wave. Neither of these features is well resolved in the data but we believe that better observations of the PV in the retrograde jets would resolve the dynamically significant reversal between the $n = 6$ critical layers.

CONCLUSION

Large-scale coherent structures such as jets, meandering jets and waves embedded in jets are characteristic features of turbulence in planetary atmospheres. While

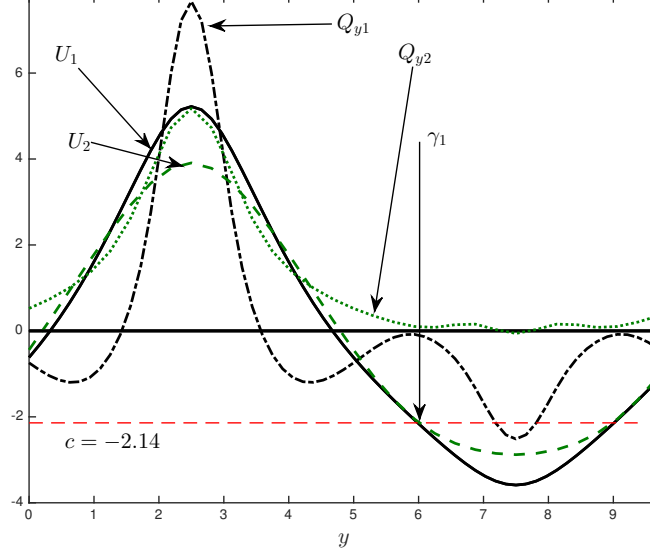


FIG. 13: For the deep stable layer NPJ S3T equilibrium shown in Fig. 9: top layer velocity, U_1 (solid), bottom layer velocity, U_2 (dashed), corresponding top layer PV gradient, Q_{y1} (dash dot) and bottom layer PV gradient, Q_{y2} (dot). Also indicated is the phase velocity of the LDM with wavenumber $n = 6$ that is the dominant perturbation in producing downgradient fluxes. Note that this LDM has eliminated the PV gradients in the vicinity of its critical layers in the top and bottom layers indicated by γ_1 . Elimination of the PV gradient at the critical layer is responsible for suppressing instability of this LDM. The strong reversal in Q_{y1} at the center of the retrograde jet resulting from the upgradient vorticity fluxes produced by the $n > 8$ waves remains as this region of PV gradient reversal is not prevented by the LDM which has been stabilized by elimination of the PV gradient at its critical layers. Such reversals are commonly observed in planetary atmospheres. Quantities are non-dimensional and parameters as in Fig. 9.

conservation of energy and enstrophy in inviscid 2D turbulence predicts spectral evolution leading to concentration of energy at large scales, these considerations cannot predict the phase of the spectral components and therefore can neither address the central question of the organization of the energy into jets with specific structure nor the existence of the coherent component of the planetary scale waves. In order to study structure formation additional aspects of the turbulence dynamics beyond conservation principles must be incorporated in the analysis. SSD models have been developed to study turbulence dynamics and specifically to solve for turbulent state equilibria consisting of coexisting coherent mean structures and incoherent turbulent components which together constitute the complete state of the turbulence. In this work an SSD two-layer baroclinic model was used to study the regime of a coexisting jet and wave in Saturn's NPJ. This second order SSD model, referred to as the S3T model, is closed by a stochastic parameterization that accounts for both the neglected nonlinear dynamics of the perturbations from the zonal mean as well as the excitation maintaining the turbulence. The equation for the zonal mean retains its interaction through Reynolds

stress with the perturbations.

In this model a jet forms as an instability and grows at first exponentially eventually equilibrating at finite amplitude. Exploiting the simplicity of the asymptotic regime in which the jet is undamped makes it possible to obtain a universal jet structure and jet amplitude scaling. Having obtained an understanding of the physical mechanism underlying this asymptotic scaling it was established that the associated amplitude scaling was necessarily robust which compelled the conclusion that the observed structure of the NPJ requires a value of β greater than the planetary value. This implied existence of a topographic beta effect with a specific predicted value. Incorporating the required poleward decreasing stable layer depth into the model produced the observed jet structure. In the model a stable retrograde mode of the Rossby wave spectrum with wavenumber six becomes nearly neutrally stable as the jet amplitude increased and by inducing strong non-normal interaction with the jet arrests its growth via perturbation Reynolds stresses. This composite structure equilibrates in the form of a hexagonal jet in agreement with the NPJ observations. Among the observational correlates of this theory is the predicted

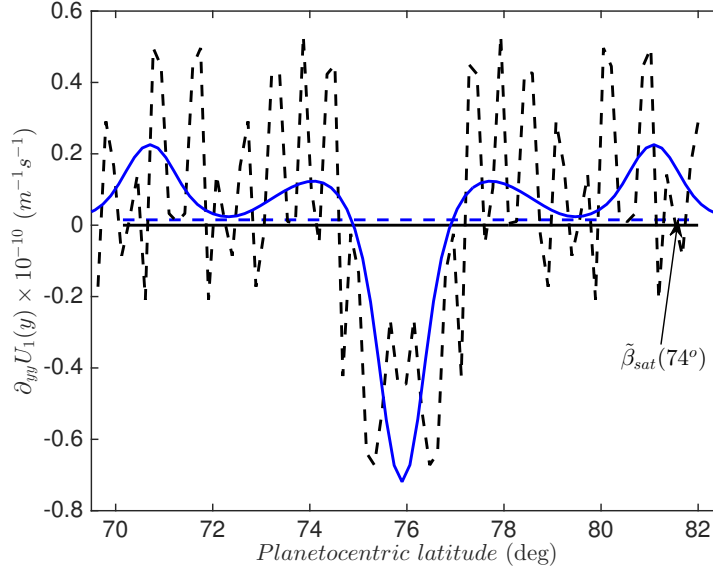


FIG. 14: The dimensional curvature of the predicted NPJ velocity structure of the top layer jet of the S3T equilibrium shown in Fig. 9 (solid) plotted against the curvature predicted by the raw data of [18] (dashed line). Also indicated is the planetary $\beta_{sat}(74^\circ)$. Note that the data suggests both the curvature reversal in the vicinity of the prograde jet, which the theory predicts to be related to the subdominant prograde mode with $c = 2.93$ that is responsible for the secondary maximum in the resolvent response in Fig. 11, and also the dynamically significant second reversal of the curvature at the retrograde section of the jet predicted by the theory to lie between the critical layers of the dominant $n = 6$ wave.

existence of robust PV gradient reversals in both the prograde and retrograde jets as well as the location and structure of these reversals.

Brian Farrell was partially supported by NSF AGS-1246929.

* pjioannou@phys.uoa.gr

- [1] A. P. Ingersoll, *Science* **248**, 308 (1990).
- [2] A. R. Vasavada and A. P. Showman, *Rep. Prog. Phys.* **68**, 1935 (2005).
- [3] A. Sanchez-Lavega, J. F. Rojas, and P. V. Sada, *Icarus* **147**, 405 (2000).
- [4] R. H. Kraichnan, *Phys. Fluids* **11**, 1417 (1967).
- [5] P. B. Rhines, *J. Fluid Mech.* **69**, 417 (1975).
- [6] G. P. Williams, *J. Atmos. Sci.* **36**, 932 (1979).
- [7] G. P. Williams, *J. Met. Soc. Jap.* **81**, 439 (2003).
- [8] R. L. Panetta, *J. Atmos. Sci.* **50**, 2073 (1993).
- [9] T. Nozawa and Y. Yoden, *Phys. Fluids* **9**, 2081 (1997).
- [10] H.-P. Huang and W. A. Robinson, *J. Atmos. Sci.* **55**, 611 (1998).
- [11] S. Lee, *J. Atmos. Sci.* **62**, 2484 (2005).
- [12] A. J. Manfroi and W. R. Young, *J. Atmos. Sci.* **56**, 784 (1999).
- [13] G. K. Vallis and M. E. Maltrud, *J. Phys. Oceanogr.* **23**, 1346 (1993).
- [14] J. Y.-K. Cho and L. M. Polvani, *Science* **273**, 335 (1996).
- [15] P. L. Read, Y. H. Yamazaki, S. R. Lewis, P. D. Williams, K. Miki-Yamazaki, J. Sommeria, H. Didelle, and A. Fincham, *Geophys. Res. Lett.* **87**, 1961 (2004).
- [16] B. Galperin, H. Nakano, H.-P. Huang, and S. Sukoriansky, *Geophys. Res. Lett.* **31**, 13303 (2004).
- [17] B. Galperin, R. M. Young, S. Sukoriansky, N. Dikovskaya, P. L. Read, A. J. Lancaster, and D. Armstrong, *Icarus* **229**, 295 (2014).
- [18] A. Antuñano, T. del Río-Gaztelurrutia, A. Sánchez-Lavega, and R. Hueso, *J. Geophys. Res.-Planet* **120**, 155 (2015), 2014JE004709.
- [19] A. Sánchez-Lavega, T. del Río-Gaztelurrutia, R. Hueso, S. Pérez-Hoyos, E. García-Melendo, A. Antuñano, I. Mendikoa, J. F. Rojas, J. Lillo, D. Barrado-Navascués, J. M. Gomez-Forrellad, C. Go, D. Peach, T. Barry, D. P. Milika, P. Nicholas, and A. Wesley, *Geophys. Res. Lett.* **41**, 1425 (2014), 2013GL059078.
- [20] A. C. Barbosa Aguiar, P. L. Read, R. D. Wordsworth, T. Salter, and Y. Hiro Yamazaki, *Icarus* **206**, 755 (2010).
- [21] A. P. Ingersoll, T. Dowling, P. J. Gierasch, G. Orton, P. L. Read, A. Sanchez-Lavega, A. Showman, A. A. Simon-Miller, and A. R. Vasavada, in *Jupiter: the Planet, Satellites, and Magnetosphere*, edited by F. Bagenal, T. E. Dowling, and W. B. McKinnon (Cambridge University Press, Cambridge, 2004) pp. 105–128.
- [22] C. Salyk, A. P. Ingersoll, J. Lorre, A. Vasavada, and A. D. Del Genio, *Icarus* **185**, 430 (2006).
- [23] A. Delgenio, J. Barbara, J. Ferrier, A. Ingersoll, R. West, A. Vasavada, J. Spitale, and C. Porco, *Icarus* **189**, 479 (2007).
- [24] R. D. Wordsworth, P. L. Read, and Y. H. Yamazaki,

- Phys. Fluids* **20**, 126602 (2008).
- [25] B. F. Farrell and P. J. Ioannou, *J. Atmos. Sci.* **60**, 2101 (2003).
 - [26] B. F. Farrell and P. J. Ioannou, *J. Atmos. Sci.* **66**, 2444 (2009).
 - [27] A. R. Vasavada, S. Horst, M. Kennedy, and A. Ingersoll, *Journal of Geophysical Research* (2006).
 - [28] P. J. Gierasch, A. P. Ingersoll, D. Banfield, S. P. Ewals, P. Helfenstein, A. Simon-Miller, A. Vasavada, H. H. Breneman, D. A. Senske, and the Galileo Imaging Team, *Nature* **403**, 628 (2000).
 - [29] E. Hopf, *J. Ration. Mech. Anal.* **1**, 87 (1952).
 - [30] B. F. Farrell and P. J. Ioannou, *J. Atmos. Sci.* **64**, 3652 (2007).
 - [31] K. Srinivasan and W. R. Young, *J. Atmos. Sci.* **69**, 1633 (2012).
 - [32] J. B. Parker and J. A. Krommes, *New J. Phys.* **16**, 035006 (2014).
 - [33] N. A. Bakas and P. J. Ioannou, *Phys. Rev. Lett.* **110**, 224501 (2013).
 - [34] N. C. Constantinou, B. F. Farrell, and P. J. Ioannou, *J. Atmos. Sci.* **71**, 1818 (2014).
 - [35] B. F. Farrell and P. J. Ioannou, *J. Atmos. Sci.* **65**, 3353 (2008).
 - [36] J. Pedlosky, *Geophysical Fluid Dynamics*, 2nd ed. (Springer, 1992).
 - [37] D. B. Haidvogel and I. M. Held, *J. Atmos. Sci.* **37**, 2644 (1980).
 - [38] T. DelSole and B. F. Farrell, *J. Atmos. Sci.* **53**, 1781 (1996).
 - [39] T. DelSole and A. Y. Hou, *J. Atmos. Sci.* **56**, 3436 (1999).
 - [40] T. DelSole, *Surv. Geophys.* **25**, 107 (2004).
 - [41] T. DelSole and B. F. Farrell, *J. Atmos. Sci.* **52**, 2531 (1995).
 - [42] A. Sánchez-Lavega, G. S. Orton, R. Hueso, E. García-Melendo, S. Perez-Hoyos, A. Simon-Miller, J. F. Rojas, J. M. Gómez, P. Yanamandra-Fisher, L. Fletcher, J. Joels, J. Kemener, J. Hora, E. Karkoschka, I. de Pater, M. H. Wong, P. S. Marcus, N. Pinilla-Alonso, F. Carvalho, C. Go, D. Parker, M. Salway, M. Valimberti, A. Wesley, and Z. Pujic, *Nature* **451**, 437 (2008).
 - [43] Y. Kitamura and K. Ishioka, *J. Atmos. Sci.* **64**, 3340 (2007).
 - [44] B. F. Farrell and P. J. Ioannou, *J. Atmos. Sci.* **66**, 3197 (2009).
 - [45] N. A. Bakas and P. J. Ioannou, *J. Atmos. Sci.* **70**, 2251 (2013).
 - [46] A. Kasahara, *J. Atmos. Sci.* **37**, 917 (1980).
 - [47] B. F. Farrell and P. J. Ioannou, *J. Atmos. Sci.* **53**, 2025 (1996).
 - [48] B. F. Farrell, *Phys. Fluids* **31**, 2093 (1988).